Angular memory effect of transmission eigenchannels: supplementary material

Hasan Yılmaz,[1] Chia Wei Hsu,[1,2] Arthur Goetschy,[3] Stefan Bittner,[1] Stefan Rotter,[4] Alexey Yamilov,[5] and Hui Cao[1,*]

[1]*Department of Applied Physics, Yale University, New Haven, Connecticut 06520, USA*
[2]*Ming Hsieh Department of Electrical and Computer Engineering, University of Southern California, Los Angeles, California 90089, USA*
[3]*ESPCI Paris, PSL University, CNRS, Institut Langevin, 1 rue Jussieu, F-75005 Paris, France*
[4]*Institute for Theoretical Physics, Vienna University of Technology (TU Wien), 1040, Vienna, Austria*
[5]*Department of Physics, Missouri University of Science & Technology, Rolla, Missouri 65409, USA*

(Dated: October 8, 2019)

This document provides supplementary information to 'Angular memory effect of transmission eigenchannels'. Here, we elaborate on the experimental setup and measurement procedure, provide details of the numerical simulations and the phenomenological model.

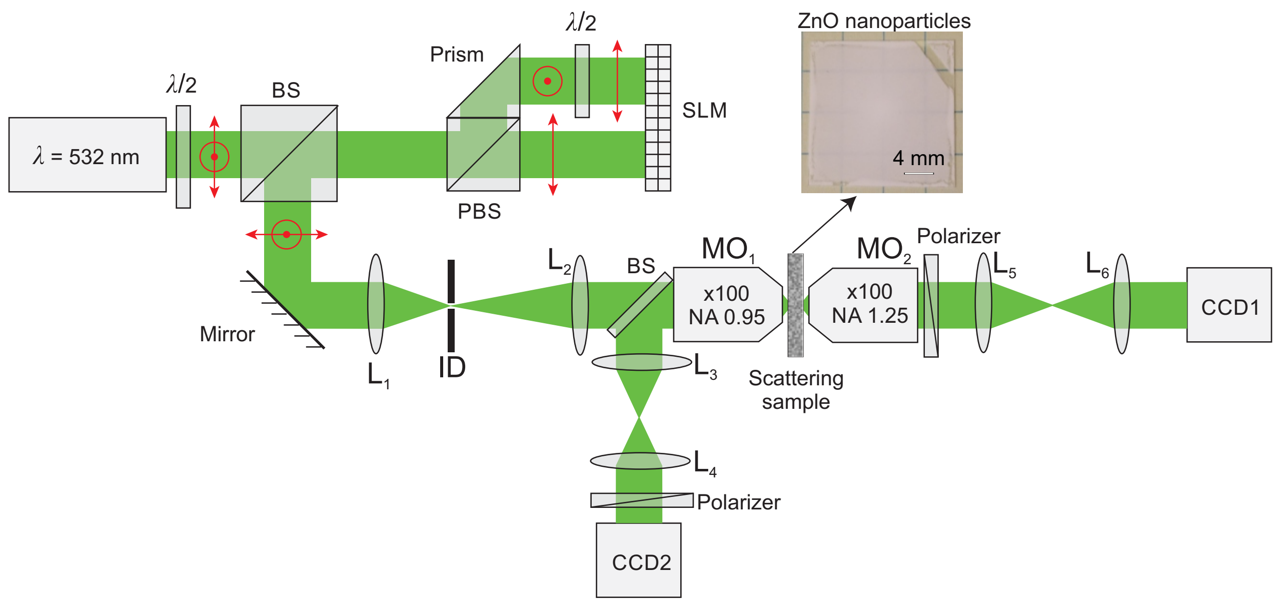

FIG. S1. A detailed sketch of the experimental setup. A reflective phase-only SLM modulates separately the phase-fronts of two orthogonal linear polarization components of a monochromatic laser beam ($\lambda = 532$ nm). The field transmission matrix of the scattering sample is measured in k space with the SLM and the camera CCD1. Inset: an optical image of the scattering sample: a 10 µm-thick film of ZnO nanoparticles on a glass substrate. The camera CCD2 captures the spatial intensity profile of reflected light in k space. $\lambda/2$: half-wave plate. BS: beam splitter. PBS: polarizing beam splitter. $MO_{1,2}$: microscope objectives. L_{1-6}: lenses. ID: iris diaphragm.

Experiment

The sample is made of densely-packed zinc oxide (ZnO) nanoparticles (average diameter $\simeq 200$ nm), deposited on a cover slip of thickness 170 µm. The average transmittance is approximately 0.2. The effective refractive index of the ZnO nanoparticle layer is about 1.4 [1], which closely matches the refractive index of the glass substrate.

---

* hui.cao@yale.edu

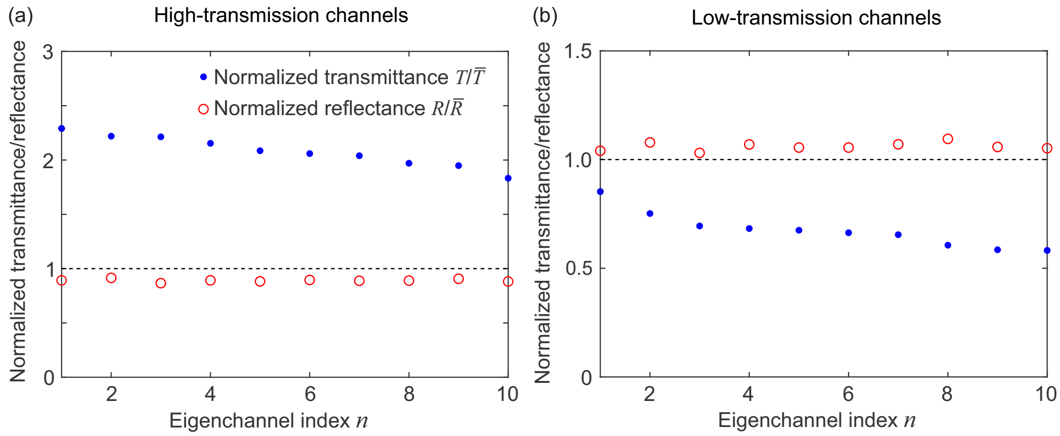

FIG. S2. Experimentally measured transmittance and reflectance of transmission eigenchannels, normalized to the values of random incident wavefronts. (a) The ten highest transmission eigenchannels all have normalized reflectance $R/\overline{R} < 1$. (b) The ten lowest transmission eigenchannels all have normalized reflectance $R/\overline{R} > 1$. The black dashed lines represent $T/\overline{T} = R/\overline{R} = 1$.

A detailed sketch of the experimental setup is presented in Fig. S1. A linearly-polarized monochromatic laser beam (Coherent, Compass 215M-50 SL) with wavelength $\lambda = 532$ nm is expanded and collimated. Its polarization direction is rotated from vertical to 45° by a half-wave ($\lambda/2$) plate, and split into vertical and horizontal polarizations by a polarizing beam splitter (PBS). The horizontal-polarized component of the beam illuminates one part of the SLM (Hamamatsu, X10468-01). Since the SLM only modulates horizontal polarization, the vertically-polarized component of the beam is converted into horizontal polarization by another $\lambda/2$ plate before impinging onto the second part of the SLM; the modulated reflected beam is converted back to vertical polarization after passing through the same $\lambda/2$ plate again. The two polarizations are recombined at the PBS, and the SLM plane is imaged onto the pupil of a microscope objective MO_1 (Nikon CF Plan 100× with a numerical aperture $NA_{in} = 0.95$) by a pair of lenses L_1 and L_2 (with focal lengths $f_1 = 100$ mm and $f_2 = 250$ mm). The reflected light from the ZnO sample is collected by the same objective MO_1, and the far-field intensity distribution on its pupil is imaged onto a camera CCD2 (Allied Vision, Mako G-032B) by a pair of lenses L_{3-4} with focal lengths of $f_3 = f_4 = 200$ mm. A linear polarizer is placed before the camera to select only one polarization of the reflected light.

In transmission, the Fourier transform of the transmitted field on the back (output) surface of the sample is imaged onto another camera CCD1 (Allied Vision, Manta G-031B) by an oil-immersion microscope objective MO_2 (Edmund Optics DIN Achromatic 100×, $NA_{out} = 1.25$) and a pair of lens L_5 ($f_5 = 200$ mm) and L_6 ($f_6 = 150$ mm). The field of view of MO_2 on the back surface of the sample has a diameter of 180 µm. A linear polarizer is placed right after MO_2 to filter out one polarization component of the transmitted light.

The field transmission matrix from the SLM to the CCD1 is measured in Hadamard basis, with a common-path interferometry method [2–4]. 4830 SLM macropixels (2415 per polarization) are imaged onto the entrance pupil of MO_1, covering the entire pupil. Among them, we use 2048 macropixels (1024 per polarization) for the signal field and 2782 macropixels for the reference field in the transmission matrix measurement. Each macropixel consists of 9×9 SLM pixels. A uniform (but fixed) phase pattern is displayed on the reference pixels. To measure the transmitted intensity of the signal field in each Hadamard basis vector, a high-spatial-frequency phase grating is written to the reference region of the SLM so that the reference field is diffracted away from the iris ID.

After measuring the field transmission matrix, we calculate the eigenvectors which represent the input wavefronts for individual transmission eigenchannels using the relation $t^{\dagger}tV_n = \tau_n V_n$, where V_n is the n-th eigenvector, and τ_n is the corresponding eigenvalue that gives the transmittance of the n-th eigenchannel. After finding the eigenvectors, we block the reference field by imposing a high-spatial-frequency phase grating on the reference region of the SLM. Then we display the phase patterns of the phase-only modulated eigenvectors with the 10 highest and lowest transmittance on the 2048 macropixels of the SLM, and record the transmitted and reflected intensity patterns with CCD1 and CCD2. The transmittance T and reflectance R for these channels are obtained by integrating the patterns, and normalized by the average values shown in Fig. S2. These data confirm that the high (or low) transmission channels have reduced (or enhanced) reflection. Next we gradually shift the phase pattern of each channel on the SLM to tilt its incident wavefront, and record the transmitted and reflected intensity patterns in far field. Each step of the tilt is about 0.2°, and the total range is 3.5°, which is significantly larger than the angular correlation width of the random wavefronts. We repeat this measurement for 20 random incident wavefronts to find the angular memory-effect range.

In principle, adding a linear phase ramp to the incident field on the sample surface by translating the SLM phase pattern does not modify the intensity pattern on the sample surface. However, due to optical aberrations in the setup, the translation in k space slightly modifies the illumination pattern on the sample surface. Such modification depends on the incident beam width on the sample surface, therefore it is different for high-transmission channels which have smaller beam width than low-transmission channels [4]. The modification of the incident intensity pattern would accelerate the decorrelation of transmitted pattern and reduce the angular correlation width. In order to have a fair comparison of the memory-effect range between random wavefronts and transmission eigenchannels, we use the phase-conjugate of the SLM phase patterns of the high/low-transmission eigenchannels as random wavefronts. The transmission eigenchannels and their phase-conjugates have equal incident beam width on the sample surface. However, the phase-conjugate inputs have a transmittance close to the average value, $T/\overline{T} = 1$, as expected from the random wavefronts. We normalize the tilt angle θ in the plot of high/low-transmission channels' intensity correlation functions by the width of their phase-conjugate incident wavefronts' intensity correlation functions, denoted as $\theta/\theta_0^{(\mathrm{r})}$ in Fig. 1(c) of the main text.

Numerical simulations

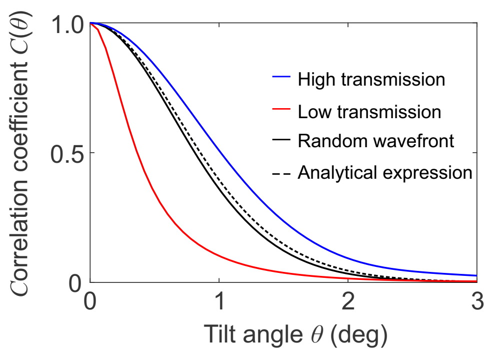

FIG. S3. Numerically calculated intensity correlation function $C(\theta)$ of transmission eigenchannels, in comparison to the random wavefronts and the analytical expression are presented. While $C(\theta)$ of random incident wavefronts (black solid line) agrees well to the analytical expression (black dashed line), an eigenchannel of $\tau_n = 0.999$ (blue solid curve) exhibits a slower decay of $C(\theta)$, while an eigenchannel of $\tau_n = 0.01$ (solid red curve) a faster decay. Each numerical curve represents an average over 10 disorder realizations. Simulation parameters are identical to those in Fig. 2 of the main text.

In our numerical simulations, we calculate wave propagation through two-dimensional (2D) diffusive slabs, $W \gg L \gg l_{\mathrm{t}}$. The sample is discretized on a 2D square grid, and the grid size is $(\lambda/2\pi) \times (\lambda/2\pi)$. The dielectric constant at each grid point is $\epsilon(\mathbf{r}) = n_0^2 + \delta\epsilon(\mathbf{r})$, where n_0 is the average refractive index of the sample, $\delta\epsilon(\mathbf{r})$ a random number between $[-\Sigma, \Sigma]$ with uniform probability. The sample is sandwiched between two homogeneous media with refractive indices of n_1 and n_2. Periodic boundary conditions are applied to the transverse boundaries. To obtain the field transmission matrix t at wavelength λ, we solve the scalar wave equation $\left[\nabla^2 + k_0^2\epsilon(\mathbf{r})\right]\psi(\mathbf{r}) = 0$ with the recursive Green's function method [5, 6].

After finding incident wavefronts from the eigenvectors of $t^\dagger t$, we calculate the output fields of each eigenchannel by tilting its incident wavefront. The transmitted field is then tilted back by the same angle θ, and its Pearson correlation with the original transmitted field is computed. From the field correlation $C_n^{(\mathrm{E})}(\theta)$, the intensity correlation $C_n(\theta) = |C_n^{(\mathrm{E})}(\theta)|^2$ is obtained. Fig. S3 shows the numerically calculated intensity correlation function $C_n(\theta)$ of random incident wavefronts and of high/low-transmission eigenchannels, as well as the analytical expression given in reference [7] with no freely adjustable parameters. While the analytical correlation function $C(\theta)$ agrees well with the $C(\theta)$ for random incident wavefronts, we observe distinct differences for the high/low-transmission eigenchannels.

We further investigate the scaling of the angular memory-effect range with the sample thickness. We numerically calculate the angular width $\theta_0^{(\mathrm{h})}$ of the intensity correlation function for the average high-transmission channels with $\tau_n > \overline{\tau}$ in diffusive slabs with different thickness L and transport mean free path l_{t}. As shown in Fig. S4, $\theta_0^{(\mathrm{h})}$ is inversely proportional to the effective sample thickness, $L_{\mathrm{eff}} = L + 2z_{\mathrm{e}}$, where $z_{\mathrm{e}} = 0.818 l_t$ is the extrapolation length for the index-matched interfaces. Hence, $\theta_0^{(\mathrm{h})}$ becomes independent of l_{t} for $L \gg l_{\mathrm{t}}$.

The slab parameters (refractive indices, transport mean free path, slab thickness) and the parameters that define incomplete channel control used in the numerical simulations for Fig. 3 of the main text, are chosen to be close to those

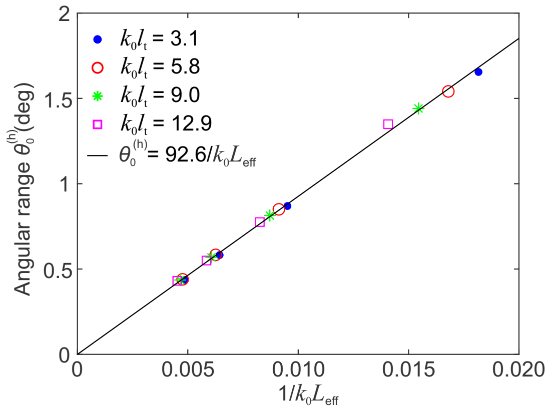

FIG. S4. Scaling of angular correlation width with sample thickness. Numerically calculated angular width $\theta_0^{(\mathrm{h})}$ of the intensity correlation function averaged over high-transmission channels with $\tau_n > \overline{\tau}$, versus the effective sample thickness, $L_{\mathrm{eff}} = L + 2z_{\mathrm{e}}$, where $z_{\mathrm{e}} = 0.818 l_t$. The slabs have different L and l_{t}, but the same width $k_0 W = 3000$ and average refractive index $n_0 = 1.5$. Each data point represents an average over 10 disorder realizations.

of our experiment with the ZnO nanoparticle layer. The slab ($n_0 = 1.4$) is sandwiched between air ($n_1 = 1.0$) and glass ($n_2 = 1.5$). In case of complete control, the number of input modes (from the air) is $M_1 = 1999 \approx 2n_1 W/\lambda$, and the number of output modes (to the glass) $M_2 = 3239$. To model the effect of incomplete control on the angular-memory effect of transmission eigenchannels, we apply the following procedures on the complete transmission matrices. Due to the limited numerical aperture (NA) in the illumination and the detection, and single polarization detection, the number of experimentally accessible columns (input modes) and rows (output modes) of the transmission matrix is reduced. To numerically model such reduction of the transmission-matrix size, we take only 1024 columns and 1155 rows of the k-space transmission matrices in our simulations. Moreover, to model the binning of SLM pixels into macropixels, we group the columns in k-space. The number of columns in one group, $m_1 = 32$, is chosen such that the corresponding illumination width on the front surface of the slab is similar to that in the experiment. Such truncation and grouping the columns effectively reduce the number of degrees of freedom to $M_1^{(\mathrm{eff})} = 32$ at the input. We did not group the output modes, since the detection field of view is larger than the beam width at the output in the experiment. To model the incomplete detection for the reflection memory effect in the simulations (Fig. 3(b) in the main text), we apply exactly the same truncation and grouping to the columns of the reflection matrices, but take only 1024 out of 1999 number of rows of the reflection matrices.

Phenomenological model

Here we present the details of our phenomonological model for the angular memory effect of transmission eigenchannels and the complete derivation of the intensity correlation function C_n in Eq. (1) of the main text.

The n-th transmission eigenchannel has the input state $|V_n\rangle$, which is associated to the transmission eigenvalue τ_n by the relation:

$$t^\dagger t \, |V_n\rangle = \tau_n \, |V_n\rangle \, . \tag{S1}$$

Here t is the field transmission matrix whose singular value decomposition reads

$$\begin{aligned} t &= U \tau^{1/2} V^\dagger \\ &= \sum_k |U_k\rangle \, \tau_k^{1/2} \, \langle V_k| \, , \end{aligned} \tag{S2}$$

so that $t\,|V_n\rangle = \sqrt{\tau_n}\,|U_n\rangle$ is the output associated to V_n.

When the diffusive slab is tilted by an angle θ, the output state becomes $t_\theta \, |V_n\rangle$. We define the intensity correlation function between the two output states as

$$\begin{aligned} C_n(\theta) &\equiv \frac{|\langle V_n| t^\dagger t_\theta |V_n\rangle|^2}{\langle V_n| t^\dagger t |V_n\rangle \langle V_n| t_\theta^\dagger t_\theta |V_n\rangle} \\ &= \frac{|\langle U_n| t_\theta |V_n\rangle|^2}{\langle V_n| t_\theta^\dagger t_\theta |V_n\rangle}. \end{aligned} \tag{S3}$$

The sample tilt is equivalent to the operation that consists in tilting the illumination wavefront by an angle θ, applying the transmission matrix t, and tilting back the scattered wavefront by $-\theta$. Thus t_θ can be expressed as

$$t_\theta = R_\theta^\dagger \, t \, R_\theta, \tag{S4}$$

where R_θ is the tilting matrix and can be written in real space as

$$R_\theta = \mathrm{e}^{\mathrm{i}k\theta\hat{\rho}}, \tag{S5}$$

where $\hat{\rho}$ represents the transverse coordinate on the front surface of the sample. For $\theta \ll 1$, $R_\theta \simeq \mathbb{1} + \mathrm{i}k\theta\hat{\rho}$, where $\mathbb{1}$ is the identity matrix. This suggests to model the tilting matrix R_θ as

$$R_\theta = \mathbb{1} + X, \tag{S6}$$

where X is an $N \times N$ complex Gaussian random matrix, whose elements satisfy the following relations in the channel basis:

$$\overline{X_{ij}} = 0, \tag{S7}$$

$$\overline{X_{ij} X^*_{i'j'}} = (\sigma^2/N)\delta_{ii'}\delta_{jj'}. \tag{S8}$$

Here the random matrix elements are averaged over ensembles. This model is phenomenological because we replace the deterministic matrix R_θ by a random matrix. According to the decompositions (S2) and (S4), and the model (S6), the numerator of the correlation function C_n becomes

$$\begin{aligned} |\langle U_n| t_\theta |V_n\rangle|^2 &= |\langle U_n| (1 + X^\dagger) t (1 + X) |V_n\rangle|^2 \\ &= |\sqrt{\tau_n} + \sqrt{\tau_n} \langle U_n| X^\dagger |U_n\rangle + \sqrt{\tau_n} \langle V_n| X |V_n\rangle + \langle U_n| X^\dagger t X |V_n\rangle|^2 \\ &= \tau_n |1 + \langle U_n| X^\dagger |U_n\rangle + \langle V_n| X |V_n\rangle|^2 + |\langle U_n| X^\dagger t X |V_n\rangle|^2 \\ &\quad + 2\mathrm{Re}\left[\left(1 + \langle U_n| X^\dagger |U_n\rangle + \langle V_n| X |V_n\rangle\right) \langle V_n| X^\dagger t^\dagger X |U_n\rangle\right]. \end{aligned} \tag{S9}$$

We expand each term in the channel basis and proceed to the average over the matrix X, using Gaussian contraction rules and Eqs. (S7) and (S8). The average of the numerator becomes

$$\overline{|\langle U_n| t_\theta |V_n\rangle|^2} = (1 + 2\sigma^2/N)\tau_n + \sigma^4\overline{\tau}/N, \tag{S10}$$

where $\overline{\tau} = \mathrm{Tr}(t^\dagger t)/N$. Similarly, the expression for the denominator of the correlation function C_n is written as

$$\langle V_n| t_\theta^\dagger t_\theta |V_n\rangle = \langle V_n| (\mathbb{1} + X^\dagger) t^\dagger (\mathbb{1} + X)(\mathbb{1} + X^\dagger) t (\mathbb{1} + X) |V_n\rangle. \tag{S11}$$

We average this expression, keeping only the terms that involve the same number of matrices X and $X^\dagger$, and using $\mathrm{Tr}(t) \simeq 0$ we obtain

$$\langle V_n| \overline{t_\theta^\dagger t_\theta} |V_n\rangle \simeq (1 + \sigma^2)(\tau_n + \sigma^2\overline{\tau}). \tag{S12}$$

Finally, by combining Eqs. (S10) and (S12), we get the following expression for the mean of the correlation function:

$$\overline{C_n} = \frac{(1 + 2\sigma^2/N)\tau_n + \sigma^4\overline{\tau}/N}{(1 + \sigma^2)(\tau_n + \sigma^2\overline{\tau})}. \tag{S13}$$

For $\sigma^2 \ll N$, $\overline{C_n}$ is well approximated by

$$\overline{C_n} \simeq \frac{1}{1 + \sigma^2} \frac{\tau_n + \sigma^4\overline{\tau}/N}{\tau_n + \sigma^2\overline{\tau}}. \tag{S14}$$

We found that this result provides a good fit of our simulations for arbitrary tilt angle θ. For $\theta \ll 1$ rad, the decomposition (S6) applies with $X \simeq \mathrm{i}k_0\theta\hat{\rho}$. Hence, we expect in this limit the scaling $\sigma^2 = \overline{\mathrm{Tr}X^\dagger X/N} \propto \theta^2$. Our numerical analysis reveals that the scaling prefactor is $\sigma^2/\theta^2 \propto (k_0 L_{\mathrm{eff}})^2$. This is consistent with the numerical results showing that the angular correlation width of the open channels scales as $\theta_0^{(\mathrm{h})} \propto 1/(k_0 L_{\mathrm{eff}})$ (see Fig. S4).

The phenomenological model can be applied to reflection matrices r, and the mean of the intensity correlation function in reflection $\overline{C_n^{(\mathrm{R})}}$ can be derived in the same way:

$$\overline{C_n^{(\mathrm{R})}} \simeq \frac{1}{1+\sigma^2}\frac{(1-\tau_n)+\sigma^4(1-\bar{\tau})/N}{(1-\tau_n)+\sigma^2(1-\bar{\tau})}. \tag{S15}$$

Hence, the reflected pattern stays more correlated for low-transmission channels (with high reflectance); when the reflection eigenvalue $\rho_n = 1-\tau_n \gg \sigma^2$, $\overline{C_n^{(\mathrm{R})}}$ approaches unity. In contrast, the reflected pattern decorrelates faster for high-transmission channels (low reflectance); for $\rho_n = 1-\tau_n \to 0$, the correlation function $\overline{C_n^{(\mathrm{R})}}$ is on the order of $1/N$, which is the expected value between two uncorrelated speckle patterns with N speckle grains. Although we do not probe the reflection eigenchannels explicitly in our experiment, we measure the reflectance of transmission eigenchannels and find that high (low) transmission channels have low (high) reflectance (Fig. S2). According to the phenomenological model, the reflection eigenchannels with high reflectance (low transmittance) have stronger correlation and larger memory effect than the eigenchannels with low reflectance (high transmittance).

[1] I. M. Vellekoop, E. G. van Putten, A. Lagendijk, and A. P. Mosk, "Demixing light paths inside disordered metamaterials," Opt. Express **16**, 67–80 (2008).

[2] S. M. Popoff, G. Lerosey, R. Carminati, M. Fink, A. C. Boccara, and S. Gigan, "Measuring the transmission matrix in optics: an approach to the study and control of light propagation in disordered media," Phys. Rev. Lett. **104**, 100601 (2010).

[3] C. W. Hsu, S. F. Liew, A. Goetschy, H. Cao, and A. D. Stone, "Correlation-enhanced control of wave focusing in disordered media," Nat. Phys. **13**, 497–502 (2017).

[4] H. Yılmaz, C. W. Hsu, A. Yamilov, and H. Cao, "Transverse localization of transmission eigenchannels," Nat. Photonics **13**, 352—358 (2019).

[5] A. MacKinnon, "The calculation of transport properties and density of states of disordered solids," Z. Phys. B **59**, 385—390 (1985).

[6] H. U. Baranger, D. P. DiVincenzo, R. A. Jalabert, and A. D. Stone, "Classical and quantum ballistic-transport anomalies in microjunctions," Phys. Rev. B **44**, 637–675 (1991).

[7] I. Freund and R. Berkovits, "Surface reflections and optical transport through random media: coherent backscattering, optical memory effect, frequency, and dynamical correlations," Phys. Rev. B **41**, 496–503 (1990).